

THE FOURIER RECONSTRUCTION OF A HEAD SECTION

L. A. Shepp and B. F. Logan
Bell Laboratories
Murray Hill, New Jersey 07974

Summary

The Fourier reconstruction may be viewed simply in the spatial domain as the sum of each line integral times a weighting function (to be chosen) of the distance from the line to the point of reconstruction. Ramachandran's linear interpolation, thought to be an approximation, is merely the choice of a particular weighting function. A modified weighting function simultaneously achieves accuracy, simplicity, low computation time, as well as low sensitivity to noise.

Using a simulated phantom, we compare the Fourier algorithm and a search algorithm, very similar but not identical to one described by Hounsfield⁴ under his conditions. The search algorithm required 12 iterations to obtain a reconstruction of accuracy and resolution comparable to that of the Fourier reconstruction, and was more sensitive to noise. To speed the search algorithm by using fewer iterations leaves decreased resolution in the region just inside the skull which could mask a subdural hematoma.

This is a corrected and expanded version of the short report.⁵ In this version our search reconstructions are of comparable quality to the Fourier reconstructions. Our earlier less accurate search reconstructions were the result of an error.

§1. Introduction

Let $f(x,y)$ be the linear attenuation coefficient at (x,y) in one fixed plane section of an object. Suppose the integrals

$$P_f(L) = \int_L f ds \quad (1)$$

along certain lines L in the plane are measured through x-ray transmission along L .

How can we obtain a good estimate, or reconstruction, $\tilde{f}(x,y)$ of $f(x,y)$?

Reconstruction algorithms are of two types:

- (a) An explicit formula is given for $\tilde{f}(x,y)$ in terms of the known $P_f(L)$.^{1,2,6,7,10,11}

- (b) A search is made for a function \tilde{f} whose projection integrals $P_{\tilde{f}}(L)$ agree with $P_f(L)$ in (1), using iterative relaxation.^{3,4,8}

In each of the cases (a) and (b) the final reconstruction \tilde{f} is in principle given by a formula, typically a linear sum of $P_f(L)$ with certain weights. In each case machine limitations preclude using these weights directly.

We first study and generalize (§2a) an algorithm of type (a) proposed by Ramachandran⁶ and based on the Fourier inversion formula. This algorithm is particularly simple and elegant and can be viewed in the spatial domain as follows: To reconstruct f at a point $Q = (x,y)$ each $P_f(L)$ is multiplied, or weighted, by $\phi(d)$ where ϕ is a weighting function of the distance $d = d(Q,L)$ from Q to L , and the result added over all lines L . Thus the weight given to each $P_f(L)$ in (1) in the reconstruction at Q depends only on the distance d from L to Q and not on the slope of L . The lines L are arranged in sets of n views with m parallel lines in each view. We see in §2a that good reconstructions will be obtained when the Fourier transform $\hat{\phi}$ of ϕ satisfies $\hat{\phi}(\omega) \neq 0$ for $|\omega| < \Omega$ where Ω is larger than the essential bandwidth of the picture f to be reconstructed.

As observed by Ramachandran,⁶ choosing ϕ to be piecewise linear between ray spacing distances results in a large savings in computation time because of a simultaneous linear interpolation (§2a). The linear interpolation was proposed in⁶ as a computational shortcut, sacrificing accuracy. However, we show piecewise-linearity of ϕ actually involves no sacrifice in accuracy because $\hat{\phi}(\omega) \neq 0$ for $|\omega| < \Omega$ is achievable simultaneously with piecewise-linearity of ϕ .

The simplicity of the Fourier algorithm (with any given weight function ϕ) allows a theoretical calculation (§3) of the noise variance in the reconstruction. Using

this we propose in §3 a modified weight function \bar{w} which yields a 6 db reduction in noise, with the same computation cost, although giving up some spatial resolution. With actual data, a compromise would be made, as shown in §3, between noise reduction and spatial resolution by choosing the value of the constant α in (27). The best value of α can only be chosen after experimentation with actual data.

The Fourier reconstruction process can be viewed (§2a) as an approximation to the following: For each of the n projections (or views), take the Hilbert transform differentiate it, form the backprojection, and then take (one half of) the average of these n backprojections. This observation is used in Appendix I to show that if $f(x,y) = 1$ for (x,y) inside an ellipse and is zero outside the ellipse, the above average using the exact Hilbert transforms of the projections of the ellipse gives a perfect reconstruction inside the ellipse and oscillates infinitely outside. This explains the observed fact⁶ and Fig. 8 that the error in the Fourier reconstruction of an ellipse is small inside the ellipse and large outside the ellipse. Since the skull is reasonably well approximated by a superposition of ellipses as in Fig. 1, we would expect the Fourier method to give small overshoot in the subdural region as is seen in Fig. 8. The oscillations in the reconstruction outside the skull are not important and can be truncated away. The oscillations outside the interior ellipses are small because the density of the interior tissues is nearly constant.

We chose a particular $f(x,y)$; Figs. 1, 2, and Table 1, which we consider a reasonable model of a section of the skull. Since f is the superposition of ellipses which have simply computable projections we computed the $P_f(L)$ directly. The Fourier reconstruction based on only 5000 different lines is shown in Figs. 3, 4, 5.

The reconstructions are displayed in several pictorial modes for different purposes. The line display (Figs. 4, 8, 9, 10) is most useful to compare accuracy and resolution. The global clues of the photo-displays (Plates 5, 6, 7) are most valuable in extracting information in the presence of noise.

Ellipses are more simply analyzable (Appendix I) but not special to the Fourier

method; any $f(x,y)$ with comparable bandwidth will be reconstructed as well. The Fourier reconstruction (Fig. 6) of a rectangle, which is less smooth and so has larger high frequency components than an ellipse, is of comparable accuracy. An attempt was made (Figs. 7) to view the Fourier reconstruction of the δ -function since any picture f is a superposition of δ -function pictures. The reconstruction of the δ -function gives the point-spread or Green's function of the algorithm.

We study one search method, given in detail in §2b and patterned closely after an interesting and practical method described by Hounsfield,⁴ but not identical to it. We generated the simulated projections under conditions imitating those of⁴, i.e., with the same numbers of projections (180×160) and unknowns (80×80). We also supposed as in⁴ a water bag surrounding the head, which has the effect of reducing by unity the densities inside the head (Table 1) and which among other advantages, allows $\bar{F} \equiv 0$ as a good initial value to start the iteration, following⁴. We further added* a subdural hematoma of density .05 over that of water (1.0) just inside the skull (Plate 2) to test the reconstructions in this important region.

The projection data was generated according to the requirements of⁴ (see detailed discussion in §2c) and the same data formed the inputs to both algorithms. The search reconstructions after various iterations are seen in Figs. 9, 10 and Plates 1-4. The Fourier reconstruction from the same data is given in Figs. 8 and Plate 2.

The pictures show that after about 12 iterations the search method produces a reconstruction of essentially equivalent accuracy and resolution as that of the Fourier reconstruction.** However, with fewer iterations of the search method, considerably lower resolution is obtained in the region just inside the skull. The subdural hematoma is not visible in the search reconstruction with 8 or fewer iterations although it is visible in the Fourier reconstruction.

*Suggested by J. B. Kruskal.

**In⁵ erroneous search reconstructions were given due to our programming error.

We compared the reconstructions by both methods with independent Gaussian pseudo-random noise added to each of the projections $P_f(L)$. It was found (Table 2) that a savings of 1.5 db in noise sensitivity over the unmodified Ramachandran method was obtained using the search method with 12 iterations. However, with the modified Fourier algorithm, Table 3 shows that a savings of 4 db (a factor of 4 in absorbed dose) over the search method with 12 iterations is obtained without losing resolution. The reconstructions at various noise levels are displayed in Plates 5, 6, 7. More detailed discussion is given in §3.

The computation times for the two methods under the conditions stated is about 2.8 minutes for the Fourier method and about 7.5 minutes per iteration of the search method on our Honeywell 6400 machine. Our implementation of the search method takes about twice as long as the method described in⁴ because we make a double pass through the grid of squares for each projection ray as described in §2b. Thus with only 5 iterations, and allowing for more efficient programming and special purpose machines, the computation time seems consistent with the times discussed for⁴ of about 4-8 minutes for the 5 iteration search reconstruction.⁴ However, as mentioned above 12 iterations would seem to be required for attaining full resolution in the subdural region. It is important to point out that the search method is limited to an 80x80 reconstruction whereas the Fourier method could use a much finer grid with correspondingly less granularity.

Thus there seems to be no advantage in using the search method over the Fourier method while the latter indicates 4 db lower noise sensitivity (in the modified form) with at least a factor of ten savings in computation time. These conclusions are consistent with those of studies made earlier under more general conditions by Herman and Rowland,⁹ and by Smith, Peters, and Bates.¹⁰

The figures and plates are discussed in detail in §5.

§2a. Ramachandran's Algorithm and its Modifications

Let $P(t, \theta)$ denote the integral of f along the line $L(t, \theta)$, i.e.,

$$P(t, \theta) = P_f(L(t, \theta)) = \int_{L(t, \theta)} f ds \quad (2)$$

where $L(t, \theta)$ is the line whose normal through the origin makes angle θ with the positive x-axis and has length t , $-\infty < t < \infty$, i.e., $L(t, \theta)$ is the line

$$x \cos \theta + y \sin \theta = t. \quad (3)$$

The basis of the Fourier algorithm is that the Fourier transform

$$\hat{P}(\omega, \theta) = \int_{-\infty}^{\infty} e^{-i\omega t} P(t, \theta) dt \quad (4)$$

of $P(t, \theta)$ is equal to the two-dimensional Fourier transform of f in polar-coordinates, i.e.,

$$\hat{P}(\omega, \theta) = \hat{f}(\omega, \theta) \quad (5)$$

where

$$\begin{aligned} \hat{f}(\omega, \theta) &= \int_{-\infty}^{\infty} \int_{-\infty}^{\infty} f(x, y) e^{-i\omega(x \cos \theta + y \sin \theta)} dx dy. \end{aligned} \quad (6)$$

If $P(L)$ is known for all lines L , then \hat{f} is given by (5) and (6) and the Fourier inversion formula then gives f as

$$\begin{aligned} f(x, y) &= \frac{1}{4\pi^2} \int_0^\pi d\theta \int_{-\infty}^{\infty} \hat{P}(\omega, \theta) e^{i\omega(x \cos \theta + y \sin \theta)} |\omega| d\omega \end{aligned} \quad (7)$$

where the $|\omega|$ comes from the Jacobian of the transformation into polar coordinates.

The inner integral in (7), with $t = x \cos \theta + y \sin \theta$ as in (3),

$$Q(t, \theta) = \frac{1}{2\pi} \int_{-\infty}^{\infty} \hat{P}(\omega, \theta) |\omega| e^{i\omega t} d\omega \quad (8)$$

is the derivative of the Hilbert transform of P ,^{12, Ch.V} because multiplying by $|\omega| = i\omega(-i \operatorname{sgn} \omega)$ in frequency corresponds to taking a derivative ($i\omega$) along with a Hilbert transform ($-i \operatorname{sgn} \omega$). The reconstruction at (x, y) by (7) is thus one-half the average of the back-projections,

$Q(x \cos \theta + y \sin \theta, \theta)$, over the values of θ . If $\varphi(t)$ is an even function for which

$$\hat{\varphi}(\omega) = |\omega| \quad (9)$$

for small ω , say for $|\omega| < \Omega$, and if $\hat{P}(\omega, \theta)$ is small for $|\omega| > \Omega$ which would be the case when f is smooth (by (5)) then we have approximately,

$$Q(t, \theta) = \frac{1}{2\pi} \int_{-\infty}^{\infty} \hat{P}(\omega, \theta) \hat{\varphi}(\omega) e^{i\omega t} d\omega \quad (10)$$

$$= \int_{-\infty}^{\infty} P(\tau, \theta) \varphi(t - \tau) d\tau. \quad (11)$$

If $P(\tau, \theta)$ is known only for $\tau = t_k = ka$, $k = 0, \pm 1, \pm 2, \dots$; $\theta = \theta_j = j\pi/n$, $j = 0, 1, \dots, n-1$ where a is the ray spacing distance between parallel rays in each view and n is the number of views, we replace integrals in (7) and (11) by sums and obtain the approximate reconstruction formula f_φ , depending on φ , given by

$$f_\varphi(x, y) = \frac{a}{2n} \sum_{j=0}^{n-1} \sum_{k=-\infty}^{\infty} P(t_k, \theta_j) \varphi(x \cos \theta_j + y \sin \theta_j - t_k) \quad (12)$$

Note the sum on k in (12) is finite, $|k| \leq 1/a$, if $f(x, y) = 0$ for $x^2 + y^2 \geq 1$ as we shall assume, since then $P(t, \theta) = 0$ for $|t| \geq 1$. Thus if m rays cover the unit circle in each view, $a = 2/m$.

The function $\varphi(d)$ in (12) is the weight assigned to the line $L(t_k, \theta_j)$ in reconstructing at (x, y) , where $d = x \cos \theta_j + y \sin \theta_j - t_k$ is the distance from the reconstruction point (x, y) to $L = L(t_k, \theta_j)$. We have seen that φ must satisfy (9) for $|\omega| < \Omega$ if f_φ is to be close to f for functions f of approximate bandwidth Ω , i.e., if $\hat{P}(\omega, \theta)$ is small for $|\omega| > \Omega$.

In computing f_φ , a great savings is possible if $\varphi(t)$ is linear for

$$t_k < t < t_{k+1}, \quad k = 0, \pm 1, \dots \quad (13)$$

Thus choosing, for example,

$$\varphi(0) = 4/(\pi a^2); \quad \varphi(ka) = -4/(\pi a^2(4k^2 - 1)), \quad k = \pm 1, \dots \quad (14)$$

and linear in the intervening intervals gives

$$\hat{\varphi}(\omega) = \left| \frac{2}{a} \sin \frac{\omega a}{2} \right| \left(\frac{\sin(\omega a/2)}{\omega a/2} \right)^2. \quad (15)$$

Since (9) holds for small $|\omega| \ll 1/a$, f_φ in (12) will accurately reconstruct functions f of essential bandwidth $\Omega \ll 1/a$. Since φ is linear in the intervening intervals, the computation time of (12) is lowered because the sums

$$\sum_{k=-\infty}^{\infty} P(t_k, \theta_j) \varphi(t - t_k), \quad |t| < 1/a \quad (16)$$

can be computed and stored. The quantities (16) represent what is to be back projected in the j^{th} view when the (x, y) point lies exactly on the line $L(t_k, \theta_j)$. In general (x, y) , lies between two such rays but by the linearity of φ , the exact value required in (12) is obtained by linear interpolation between the values of (16) for the two rays adjacent to (x, y) . Moreover, the linear interpolation is done simultaneously for the whole sum.

A rough estimate of the number of basic operations (multiplications) used in (12) is as follows: for each of n views we compute the quantities (16) (m^2 operations) and then back-project over K^2 points, allowing say 4 operations for each point. This gives $\approx n(m^2 + 4K^2)$ operations, which is consistent with experience. If linear interpolation is not used,¹ (12) requires nmK^2 evaluations of φ which is much larger and better reconstructions are not obtained. Two fast Fourier transforms could be used to perform the convolution in (16), which however leads to somewhat decreased accuracy unless aliasing is avoided (which in turn increases the computation cost). In any case not much time is actually saved with the fast Fourier transform since the back-projecting must be done anyway and this is at least as time-consuming as computing (16). This was also mentioned in⁶, see however¹⁰.

The particular choice of φ used in⁶ was oscillatory and leads to somewhat more oscillations in the reconstruction than is desirable. It also has a somewhat larger noise amplification factor (§3).

In §3 we give the noise amplification factor for a general weight function φ , and give a modified φ , namely

$$\bar{\varphi}(t_k) = .4\varphi(t_k) + .3\varphi(t_{k+1}) + .3\varphi(t_{k-1}) \quad (17)$$

which further decreases (by 6 db) the effect of noise in the reconstruction by essentially performing a spatial averaging (with some loss of spatial resolution).

We remark that replacing the line integrals (1) by averages ((19) below) over strips of width $w > 0$ is equivalent to replacing f by a smoothed version f^* and using line integrals (1) for f^* . This decreases the bandwidth of f and produces smoother reconstructions.

§2b. A Particular Search Algorithm

In the search method^{3,4,8} we attempt to construct a function \bar{F} using relaxation for which

$$|P_f(S) - P_{\bar{F}}(S)| \text{ is small} \quad (18)$$

where $P_f(S)$ is the average of $P_f(L)$ over the strip S of width w ,

$$P_f(S) = \frac{1}{w} \int \int_S f \quad (19)$$

We seek a function $\bar{F}(x,y)$ constant on each of an 80×80 grid of squares containing the support of f . Starting with some initial \bar{F} (which we took to be $\bar{F} \equiv 0$ as in⁴) each strip is considered in turn. On the first pass through the grid the current value of the integral (19) for the given strip under examination is computed, weighting each square by its area of intersection with the given strip. This area of intersection is determined if we know both the distance d from the center of the square to the center line of the strip S and the slope of the center line of S . Because of time limitations we do not compute this area but approximate it using the nearest value of d in a table look up of 80 values computed beforehand for each view (slope of S) and stored on disk. These 80 values are read in at the time the 160 projection values are read in for each view. On the second pass through the grid, the difference between the current value of the integral of \bar{F} for the given strip, computed above on the first pass through the grid, and the stored true value (19) is assigned to each square of the grid weighted according to the area of intersection of S with the square, using the weights as before. On each pass only those squares

are visited for which d is small. The next strip is then considered. Passing through all the strips, arranged in 180 views with 160 strips/view, constitutes one iteration. In⁴ the weights seem to be independent of the view. We have not attempted to see if this makes a difference. We used a pseudo-random ordering of the views as suggested in⁴, taking 37° between consecutive views. Varying the number of rays or the widths did not cause unstable changes in the reconstructions.

§2c. An Experimental Comparison of the Methods of §2a and §2b

We used f of Figs. 1, 2 and Table 1 except that a subdural hematoma of density (1.05) was added just inside the skull (Plate 2). We also supposed a water bag to surround the head which has the effect (after a subtraction) of reducing each of the densities of f in Table 1 by unity. The water bag is used in⁴ and permits $f \equiv 0$ to be a good initial approximation to the reduced densities and a starting value for the iteration. The $180 \times 160 = 28,800$ projection integrals (19) were computed exactly using 160 strips in each view placed over a circle of radius $\sqrt{2}$ about the origin of Fig. 1 and of width equal to $1/2$ the ray-spacing distance. Thus the strips do not overlap but only half-cover the circle of radius $\sqrt{2}$.

Both methods §§2a,b were applied to the same data. Reconstructions by the search method after various numbers of iterations are seen in Figs. 9, 10 and Plates 1-4, and may be compared with the Fourier reconstruction Fig. 8 and Plate 2. Metric distances between the matrix of reconstructed values and the original function f are given in Table 2 for the various iterations of the search method, and for the Fourier method with ϕ as in (14) and in (17).

We see from Table 2 that the Fourier method without noise filtering is only slightly closer in each metric to the original than any of the 16 search iterations. We stopped at 16 iterations, when the changes (Table 2) become very small. The distance between the Fourier without noise filtering and the later iterations of the search is quite small (Table 2). Noise filtering

increases the distance from the original picture.

In any linear method, the effect of additive noise in the projections can be isolated by inputting pseudo-random standard normal variates as the projections (19) and computing the reconstructions. The empirical root mean square of the reconstructed values will give the numerical factor by which noise in the projections is increased or decreased by the given method. Because of the simplicity of the Fourier method, this factor can also be determined theoretically (20) and (25) below, and the empirical and theoretical values agree to reasonable accuracy. We know of no way to theoretically obtain the factors for the search method. Table 3 gives these noise amplification factors for the Fourier and search methods after various iterations; A_1 is the average of the absolute values of the 80×80 reconstruction values, A_2 is their root mean square, and A_3 is the maximum of their absolute values.

We see from Table 3 that the 12th iteration of the search method has 20% smaller noise amplification factor A_2 than the Fourier method with no noise filtering. With noise filtering the Fourier method has 50% smaller noise amplification than the 12th iteration of the search method, which is a savings of 4 db. The 4th iteration of the search method has about the same value of A_2 as the Fourier method \bar{F} with the weight function $\bar{\varphi}$ (noise-filter) of §3. We see (Plate 2) that even the 8th iteration however, leaves decreased resolution in the subdural region. The amplification factors A_3 are rather larger for the search method than for the Fourier method.

We obtained the reconstructions of the original phantom by both methods with the projection integrals (19) having additive Gaussian noise with standard deviation σ . In each case the noise and picture were reconstructed separately and then combined for various σ values ($\sigma = .0005, .001, .002, .004$) to save computation costs; here we are exploiting the linearity of the methods. The resulting reconstructions are given in Plates 5-7.

It should be pointed out that the device⁴ was appropriately designed for the search method; in designing a device for the Fourier method several purely mechanical changes would be recommended:

- (a) Fewer views are required than 180; 90 would suffice and as Figs. 4 and 8 show even 50 would do.
- (b) The output array of 80×80 which is about maximal under present computer limitations with the search method could be increased to 100×100 easily or even to 200×200 without increasing memory (computation time would increase but would still be less than that of the search method).
- (c) The water bag is not required for the computation, although it does have another advantage mentioned in⁴ in that it, together with a plastic ring⁴ which squares off the circular water bag, provides a small range over which the measurements need be linear. If the water bag is omitted, the need to use additional rays to cover a circle of radius $\sqrt{2}$ is also avoidable in Fourier method however.

§3. Measurement Requirements and the Effect of Noise

The inputs to the Fourier algorithm are the numbers $P_f(L)$ in (1). In practice $P_f(L)$ is imperfectly obtained because there are statistical fluctuations in the number of photons emitted, transmitted, and detected. We model this effect by assuming independent Gaussian variables with common variance σ^2 added to each $P_f(L)$.

In Appendix II we attempt to relate σ to the expected numbers \bar{E} and \bar{D} of photons emitted and detected in each measurement, obtaining in (A21), $\sigma^2 = 4/\bar{D} \log^2(\bar{D}/\bar{E})$, see also¹³, p. 263.

Since the reconstruction formula (12) is linear and simple we can compute the theoretical standard deviation, σ_φ , in the reconstruction f_φ . We will obtain

$$\sigma_\varphi^2 = \frac{\sigma^2}{2mn} \int_{-\infty}^{\infty} \varphi^2(u) du \quad (20)$$

where n is the number of views and m is the number of rays/view which pass through the

unit circle (on which f is assumed supported).

To prove (20) suppose that

$$Q_{kj} = P(t_k, \theta_j) + \sigma \eta_{kj} \quad (21)$$

is used in (12) in place of $P(t_k, \theta_j)$ where η_{kj} are independent with zero mean and unit variance. The reconstruction (12) has mean $f_\varphi(x, y)$ as in (12) and variance σ_φ^2 given by

$$\sigma_\varphi^2 = \frac{a^2}{4n^2} \sum_{j=0}^{n-1} \sum_{k=-\infty}^{\infty} \sigma^2 \varphi(x \cos \theta_j + y \sin \theta_j - t_k) \quad (22)$$

since the errors $\sigma \eta_{kj}$ are uncorrelated. Since the average over z of the sums

$$a \sum_{k=-\infty}^{\infty} \varphi^2(z - t_k) = \int_{-\infty}^{\infty} \varphi^2(u) du \quad (23)$$

we obtain (20), since $a = 2/m$.

For the weight φ in (14), a calculation shows

$$\int_{-\infty}^{\infty} \varphi^2(u) du = a^{-3} \quad (24)$$

so that

$$\sigma_\varphi^2 = \frac{m^2 \sigma^2}{16n} \quad (25)$$

It is clear from (20) that other choices of φ will lead to reconstruction formulas that are less effected by noise. Indeed reducing

$$\int_{-\infty}^{\infty} \varphi^2(u) du = \frac{1}{2\pi} \int_{-\infty}^{\infty} |\hat{\varphi}(\omega)|^2 d\omega \quad (26)$$

will reduce the noise amplification factor σ_φ/σ in (20). However, this reduction is inconsistent with keeping $\hat{\varphi}(\omega) = |\omega|$ for $|\omega| < \Omega$ in (9). Reducing Ω magnifies the noise less, but does not permit accurate reconstruction of pictures f of bandwidth Ω . The original tomographic reconstruction method merely averages $P_f(S)$ over all strips S which pass through the point (x, y) . The variance of the reconstruction is then only σ^2/n , much smaller than (25) since m is large, but the reconstruction with no noise is poor because this method gives (approximately) the right side of (7) with the factor $|\omega|$ replaced by unity, i.e., (9) fails.

We next consider changing φ slightly to affect some noise reduction. We

will change φ by taking as a new weighting function

$$\bar{\varphi}(t) = \alpha \varphi(t) + \beta \varphi(t+a) + \beta \varphi(t-a) \quad (27)$$

where φ is as in (14). So long as

$$\alpha + 2\beta = 1 \quad (28)$$

we will have $\varphi(\omega) = |\omega|$ for small ω . Also $\bar{\varphi}$ is piecewise linear between $t_k = ka$. A calculation shows

$$\int_{-\infty}^{\infty} \bar{\varphi}^2(t) dt = a^{-3} (3\alpha^2 - 4\alpha\beta + 5\beta^2) / 3 \quad (29)$$

which is minimized by setting $\alpha = .36$, $\beta = .32$ for which $\sigma_{\bar{\varphi}}^2/\sigma_\varphi^2 = .147$. In Plates 5, 6, 7 we used $\alpha = .4$, $\beta = .3$ as in (17) which gives

$$\sigma_{\bar{\varphi}}^2 = .15 \sigma_\varphi^2 \quad (30)$$

where σ_φ^2 is given by (25). Note that the use of $\bar{\varphi}$ (in (17)) instead of φ (in (14)) in (12) is essentially performing a spatial averaging or low pass filtering since convolving $P(t_k, \theta_j)$ with $\varphi(t_{k+1})$ instead of $\varphi(t_k)$ amounts to moving the head one ray-spacing distance. Thus $f_{\bar{\varphi}}$ is roughly equivalent to averaging the reconstruction f_φ over a circle of about a ray-spacing distance a . This somewhat spoils the resolution as is clear from Plate 7 but saves a factor of $1/.15 = 6.7$ db in noise.

The quantities σ and σ_φ are dimensionless and give the theoretical determination of the noise amplification factors found empirically in §2c. For the experiment described in §2c, $\sigma = 1$, $n = 180$, and $m = 160/\sqrt{2}$ since this value of m is the number of rays which cross the unit circle on which f is supported. The second column of the last 2 rows in Table 3 are obtained with these values from (25) and (30). The first column of the last 2 rows is the mean of the absolute value of a normal random variable whose standard deviation is the second column and so is $(2/\pi)^{1/2}$ times the second.

We simulated a divergent beam using the average of 15 line integrals passing through a focal point and filling at equal angles a sector about the line L for each $P_f(L)$. It was found that even with a 4° sector of spread with the focal point situated

on the line $L(1,\theta)$, tangent to the unit circle in Fig. 1, for rays in the direction θ , completely acceptable reconstructions result using (12). In fact, the divergent beam introduces smoothing of the reconstruction. The explanation for this fortunate stability is that using divergent beams is the same as rotating the head through a (4°) angle as each measurement is taken, or equivalently averaging the reconstructions of the section in all the rotated positions. Of course this spatial averaging produces smoothing. (Similarly, using a parallel beam of nonzero width as in (19) is the same as translating the head and averaging the reconstructions of the translations, again producing smoothing.) It may be difficult to move the focal spot of the x-ray source along a line tangent to the unit circle because at the point of tangency it is too close to the head. Instead, moving the focal spot along $L(2,\theta)$, i.e., along a line tangent to the circle of radius 2 (10 cm further away) about the origin produced essentially as little distortion with a 2° sector of spread. Thus distortion due to divergent beams seems to present no serious problem.

Simulation showed that the Fourier algorithm is stable under uniform 1% errors in centering t_k (i.e., $t_k = ka + .01 \cdot a \cdot u_k$ where u_k are independent and uniformly distributed on $(-1,1)$ pseudo-random numbers) and under uniform 10% errors in centering θ_j (i.e., $\theta_j = (j + .1u_j)\pi/n$, with u_j as before).

A source of error not analyzed is that due to nonmonochromaticity of the photons in the beam.

It should be mentioned that although various ad hoc sampling theory ideas suggested ways of choosing in advance the parameters n = number of views and m = number of rays/view, we were unable to achieve sufficiently satisfying quantitative agreement with the estimates obtained. Instead $n = 50$, $m = 100$ were found empirically to produce good results for reconstructing such f as in Fig. 1 although $n = 36$, $m = 100$ also works quite well. It appears as indicated by the mathematics of Appendix I that further increasing n and m , once large enough, does

not produce large changes in the reconstruction inside the skull as indicated in comparing Fig. 4 and Fig. 8.

§4. Discussion of Figures

Figure 1 represents the particular simulated head section $f(x,y)$ used to test the Fourier algorithm. The skull was taken to have density 2 and is slightly thicker at the forehead while the interior density varies very little, between 1.0 (water) in the ventricles, 1.02 in the gray matter, to 1.03 and 1.04 in the various tumors. All of the shapes are ellipses with centers, orientations, axes, and gray levels given in Table 1. In the comparison §2c of the Fourier and search algorithms, a blood clot was added just inside the skull centered at $(.56, -.4)$ with major and minor axes, .2 and .03 with inclination $\theta = 39^\circ$ and density 1.05. The densities were then reduced by unity relative to a water bag of density 1.0 surrounding the head.

Figure 2 is a perspective plot 80×80 of $f(x,y)$ truncated at levels .9 and 1.1 for ease of comparison with later reconstructions. The effect of the truncation is discussed further in Fig. 5 below.

Figure 3 gives the reconstruction by the modified Ramachandran algorithm, (12) and (14), from 5000 projection integrals ($n = 50$ views; $m = 100$ lines/view). Instead of line integrals (1), strips as in (19) were used which were abutting (width $w = a = 2/m$) in each view. However, essentially the same reconstruction is obtained using line integrals (1).

Figure 4 gives (a more quantitative view of) the reconstruction of Fig. 3 plotted along the horizontal line $y = -.605$ which goes through the centers of the three small tumors (density (1.03)) of Fig. 1. The diameter of the small circular tumor is 4.6 mm on the human scale, considering the diameter of the unit circle to correspond to 20 cm. Again we have truncated at levels .9 and 1.1. Note the quantitative accuracy of the reconstruction.

Figure 5 shows the effect of the truncation at levels .9 and 1.1 in the earlier figures. Here we see the Fourier

reconstruction of Fig. 3 without truncation. Note the variations within the skull are only 1-4% of height of the skull and are hidden. The thicker forehead appears higher on the left.

Figure 6a is the Fourier reconstruction of a rectangle centered at the origin and oriented parallel to the axes with north-east corner at (.69, .92), along the line $y = .2$. The projection angles were $\theta_j = (j+.5)\pi/n$, $j = 0.1, \dots, n-1$ with $n = 50$, $m = 100$ with lines used instead of strips. The probable reason that the reconstruction of the rectangle is not as good as that of the ellipse of Fig. 4 is that the rectangle has more bandwidth than the (smoother) ellipses. In Fig. 6b the reconstruction is better, here $n = 90$, $m = 160$.

Figure 7a shows the point spread function for the algorithm (12) with ϕ as in (14) when projection integrals (19) over abutting strips with width $w = a$ are used. Plotted is $f_\phi(x, y)$ when f is a δ -function at the point $(x', y') = (.1, .23)$ as a function of r , $x = x' + r$, $y = y'$. That is, we see the reconstruction of a δ -function centered at (.1, .23) along a (horizontal) ray emanating from (.1, .23). Thus we have the Green's function of (12), i.e., what a picture element at (x', y') produces in the reconstruction at (x, y) . Note that using a δ -function at (x', y') and strip integrals (19) means that in each view exactly one of the projection strip integrals (19) has a nonzero value $(1/w)$.

Although Fig. 7a does have the appearance of our idea of a δ -function as it should with a perfect reconstruction scheme, if we look at $f_\phi(x' + r \cos \theta, y' + r \sin \theta)$ as in Fig. 7b with $r = .1$ as a function of θ , $0 \leq \theta \leq 2\pi$ we see that although the amplitude of the Green's function is small its oscillations are quite wild. Moreover, as r increases the frequency of oscillations increases roughly proportionately. Thus the algorithm (12) does require smoothness of f for the oscillations to cancel out in the reconstruction of a smooth superposition f of δ -functions. Similar results hold for points other than (.1, .23).

Figure 8 is the Fourier reconstruction using ϕ in (14) of the head section of Fig. 1 with a water bag added as described in §2c, using 180 views, with 160 rays/view covering a circle of radius $\sqrt{2}$ as in the scheme of ⁴. The granularity of this 80 point plot somewhat spoils the display but the accuracy interior to the skull is orders of magnitude better than that outside. This is discussed in Appendix I. The reconstruction in Figs. 4 and 8 are along essentially the same line, $y = -.60$. In Fig. 4 only 5000 integrals were used and no water bag.

Figure 9 is the search reconstruction after 4 iterations using the same data as in Fig. 8 along the same line. The reconstruction is significantly better outside the skull but of lesser quality inside. The skull is considerably thickened.

Figure 10 is the search reconstruction after 12 iterations along the same line as in Figs. 8 and 9. The reconstruction is of lesser quality outside the skull but has improved inside.

In the plates, the original head sections and reconstructions appear in an 80x80 photo-display. This display is obtained by a photodensitometer with 256 nominal gray levels to convert the 80x80 matrix of numbers, truncated at levels 0 = white and .1 = black and is similar to the method of ⁴ using a CRT.

Conclusions from the Pictures

From Plate 2 it is clear that 8 iterations (upper right) of the search reconstruction gives reasonable reconstructions inside the skull but the subdural region has low resolution. The Fourier method (lower left) is of slightly better quality overall and has better resolution in the subdural region.

Later (12-16) iterations (Plate 4) shows that the final search reconstruction (lower left) and Fourier reconstruction (lower right) are not much different.

It appears from Plates 5 and 6 that the search and Fourier unfiltered reconstructions are about equally sensitive to noise.

Plate 7 shows significant noise reduction with only moderate loss of spatial

resolution in the filtered Fourier reconstruction.

References

1. Bracewell, R. N. and Riddle, A. C. (1967). Inversion of fan-beam scans in radio astronomy. *Astrophys. J.* 150, 427-434.
2. Cho, Z. H. et al. Computerized image reconstruction methods with multiple photon/x-ray transmission scanning. Same issue of this journal.
3. Gordon, R., Bender, R., and Herman, G. (1970). Algebraic reconstruction techniques (ART) for three-dimensional electron microscopy and x-ray photograph. *J. Theor. Biol.* 29, 471-481.
4. Hounsfield, G. N. (1972). A method of and apparatus for examination of a body by radiation such as x or gamma radiation. The Patent Office, London, Patent Specification 1283915.
5. Shepp, L. A. and Logan, B. F. (1974). Reconstructing interior head tissue from x-ray transmissions, *IEEE Trans. Nucl. Sci.*, NS-21, 228-236.
6. Ramachandran, G. N. and Lakshminarayanan, A. V. (1971). Three-dimensional reconstruction from radiographs and electron micrographs: application of convolutions instead of Fourier transforms. *Proc. Natl. Acad. Sci. U.S.* (68), 2236-2240.
7. Mersereau, R. M. and Oppenheim, A. Digital reconstruction of multi-dimensional signals from their projections, *Proc. IEEE*, to appear.
8. Gilbert, P. (1972). Iterative methods for the reconstruction of three-dimensional objects from projections. *J. Theor. Biol.* 36, 105-117.
9. Herman, G. and Rowland, S. Three methods for reconstructing objects from x-rays: a comparative study. *Computer Graphics and Image Processing*, to appear.
10. Smith, P. R., Peters, T. M., and Bates, R. H. T. (1973). Image reconstruction from finite numbers of projections, *J. Phys. A*, 361-382.
11. Marr, R. B. (1974). On the reconstruction of a function on a circular domain from a sampling of its line integrals, *J. Math. Anal. and Appl.*, 357-374.
12. Titchmarsh, E. C. Introduction to the theory of Fourier integrals, 2nd ed. Oxford, 1937.
13. Gardner, R. P., Ely, R. L. Jr. Radio-isotope measurement applications in engineering, Reinhold Publishing Corp., New York, 1967.

APPENDIX I

We show in this appendix that the derivative of the Hilbert transform $Q(t, \theta)$ in (8) of an ellipse is constant inside the support of the projection of the ellipse and has infinite singularities at the outside edges of the support. This explains the phenomenon (see §1) particularly apparent in Fig. 8 of the much greater overshoot outside than inside the ellipse in the Fourier reconstruction (see §2a) where an approximate derivative of the Hilbert transform operation is used.

The projection $P(t) = P(t, \theta)$ of an ellipse of density one centered at the origin is

$$P(t) = \begin{cases} 2(a^2 - t^2)^{1/2} & , |t| \leq a \\ 0 & , |t| > a \end{cases} \quad (A1)$$

where $a = a(\theta)$ is the half-width of the projection in direction θ . We will show that $\bar{Q}(t) = \bar{Q}(t, \theta)$, the derivative of the Hilbert transform of P is given by

$$\bar{Q}(t) = \begin{cases} 2 & , |t| \leq a \\ 2-t|t| (t^2 - a^2)^{-1/2} & , |t| > a \end{cases} \quad (A2)$$

It follows from^{12, Ch. V}, that if $\phi(z)$ is a function analytic in the upper-half plane, $\text{Im } z > 0$, tending to zero sufficiently fast as $\text{Im } z \rightarrow \infty$ and

$$P(t) = \text{Re } \phi(t+i0) \quad (A3)$$

then the Hilbert transform $H(t)$ satisfies

$$H(t) = \text{Im } \phi(t+i0) \quad (A4)$$

Since the analytic function

$$\phi(z) = 2((a^2 - z^2)^{1/2} + iz) \quad (A5)$$

satisfies (A3) where P is given by (A1) and tends to zero as $z \rightarrow i\infty$, we have from (A4),

$$H(t) = \begin{cases} 2t & , |t| < a \\ 2t - 2(t^2 - a^2)^{1/2} \text{sgnt}, & |t| > a. \end{cases} \quad (A6)$$

The derivative of the Hilbert transform of P ,

$$Q(t) = H'(t) \quad (A7)$$

thus satisfies (A2).

For any f , formula (12) is essentially the same as (it would be the same from (10) and (11) if $m \rightarrow \infty$ and $\phi(\omega) = |\omega|$ for $|\omega| < \infty \rightarrow \infty$),

$$f_{\varphi}(x,y) \doteq \frac{1}{2n} \sum_{j=0}^{n-1} \overline{Q}(x \cos \theta_j + y \sin \theta_j, \theta_j) \quad (A8)$$

Thus from (A2) if $a_j = a(\theta_j)$ is the half-width of the projection of an ellipse f of density one we have

$$f_{\varphi}(x,y) \doteq 1 - \frac{1}{n} \sum |t_j| (t_j^2 - a_j^2)^{-1/2} \quad (A9)$$

where the sum is over those values of j where

$$t_j = t_j(\theta_j) = x \cos \theta_j + y \sin \theta_j \quad (A10)$$

satisfies

$$|t_j| \geq |a_j| \quad (A11)$$

If (x,y) is inside the ellipse (A11) holds for no value of j and so from (A9)

$$f_{\varphi}(x,y) \doteq 1 \quad (A12)$$

i.e. essentially exact reconstruction holds.

If instead (x,y) is outside the ellipse and on or near a line

$$x \cos \theta_j + y \sin \theta_j = \pm a_j \quad (A13)$$

then $f_{\varphi}(x,y)$ is very large and negative. Of course f_{φ} remains bounded since (A8) is only approximate when $\varphi(\omega) < |\omega|$ for large ω as must be the case, but for any good φ , we would expect large oscillations outside the ellipse and accurate reconstruction inside the ellipse (as indeed is the case in Fig. 8).

For an object such as the skull which is nearly a superposition of ellipses, but not exactly, we would expect to obtain good reconstructions inside the skull because ellipses are not special to the general theory (2)-(12). Indeed for a rectangle, which is really quite far from an ellipse, having probably much more bandwidth, similar results obtain (Figs. 6).

APPENDIX II

We attempt to relate σ in (21) to measured quantities. We suppose that each measurement is made through a common length λ of inhomogeneous material whose attenuation coefficient $\mu = \mu(x,y)$ is close to that of water, μ_w , for a given photon energy. To deal in dimensionless quantities we set

$$s = 2\ell/\lambda, \quad -\frac{\lambda}{2} < \ell < \frac{\lambda}{2} \quad (A14)$$

where ℓ measures length along the line L in (1) of length λ , so that s is dimensionless

and $-1 \leq s \leq 1$. Further the function f in (1) is dimensionlessly given by

$$f = \frac{\mu}{\mu_w} - 1 \quad (A15)$$

and corresponds to the reduced densities in §2c.

If D and E are the measured numbers of detected and omitted photons in each measurement then

$$Q = \frac{2}{\lambda \mu_w} \log(D/\overline{E}) - 2 \quad (A16)$$

is an estimate of $P_f(L) = \int f ds$. Indeed D is given by the normal approximation

$$D = \overline{D} + \eta \sqrt{\overline{D}} \quad (A17)$$

where \overline{D} is the average of D and η is standard normal. Thus

$$Q = -\frac{2}{\lambda \mu_w} \log \left[p \left(1 + \frac{1}{\sqrt{p \overline{E}}} \eta \right) \right] - 2 \quad (A18)$$

with p the probability of an emitted photon being detected given by

$$p = \overline{D}/\overline{E} = \exp \left[- \int \mu dt \right]. \quad (A19)$$

Thus from (A14), (A15), (A18), and (A19) for large \overline{D} and \overline{E} ,

$$Q \doteq \int f ds + \frac{2\eta}{\lambda \mu_w \sqrt{\overline{D}}} \quad (A20)$$

and we see that σ in (21) is given by

$$\sigma^2 = \frac{4}{\overline{D}(\lambda \mu_w)^2} \doteq \frac{4}{\overline{D}(\log \overline{D}/\overline{E})^2} \quad (A21)$$

We have used the approximation $\mu \approx \mu_w$ to obtain

$$\lambda \mu_w = \int \mu dt = \log \overline{D}/\overline{E} \quad (A22)$$

in (A21). Note that the factor of 2 in (A18) is due to s having a range of 2, $-1 \leq s \leq 1$, in dimensionless units.

In an earlier version of this paper an incorrect formula for σ^2 as $1/\overline{D}$ was given instead of (A21).

APPENDIX III

We have been asked to give the simple Fortran program below which calculates $f_{\varphi}(x,y)$ in (12) with φ as in (14). In it the quantity PHI(K+1) is actually $\varphi(K \cdot a) \cdot a/2n$. The reconstruction is stored in the Z array where $Z(i,j) = f_{\varphi}(c_i, c_j)$ where for $i=1, \dots, NX=NY=80$,

$$c_1 = -XPOS + 1.2 \cdot XPOS/NX.$$

The numbers PROJ(K) are read from a file; after the jth call to the file the number $P(t_k, \theta_j) = PROJ(K)$ where $t_k = -1 + k \cdot a$, $k = 1, \dots, m = 2/a = 100$ and $\theta_j = j\pi/n$, $n=50$ views. The convolution (or approximate Hilbert transform) is stored in CONV for each view. Steps 350-430 perform the linear interpolation. The truncation 470-500 of z to the range .9 and 1.1 could be omitted.

Note that we are using mixed integer and real modes so that e.g., in step 400, L is the integer part of R; this is needed in the interpolation step 420.

```

10  DIMENSION PHI (100),PROJ(100),CONV(100)
20  DIMENSION Z(80,80)
30  XPOS=.99
40  YPOS=.99
50  NY=80
60  NX=80
70  PI=3.14159265
80  N=50
90  M=100
100 A=2./M
110 PIN=PI/N
120 C2=-1/(2*PI*A*N)
130 DELTA=2*XPOS/NX
140 *****
150 PHI(1)=2/(PI*A*N)
160 DO 10 K=1,M-1

```

```

170 PHI(K+1)=C2/(K*K-.25)
180 10 CONTINUE
190 *****
200 DO 20 J=1,N
210 THETAJ=(J-1)*PIN
220 COSTHTAJ=COS(THETAJ)
230 SINTHTAJ=SIN(THETAJ)
240 COSDELOA=COSTHTAJ*DELTA/A
250 READ(12) (PROJ(K),K=1,M)
260 *****
270 DO 30 KR=1,M
280 CONV(KR)=0
290 DO 40 K=1,M
300 KABS=IABS(KR-K)+1
310 CONV(KR)=CONV(KR)+PROJ(K)*PHI(KABS)
320 40 CONTINUE
330 30 CONTINUE
340 *****
350 DO 51 IY=1,NY
360 Y1=-YPOS+2*YPOS*IY/NY
370 R=(-XPOS*COSTHTAJ+SINTHTAJ*Y1+1)/A
   -COSDELOA
380 DO 50 I=1,NX
390 R=R+COSDELOA
400 L=R
410 IF(L.LE.0.OR.L.GE.M) GO TO 50
420 Z(I,IY)=Z(I,IY)+(L+1-R)*CONV(L)+(R-L)
   *CONV(L+1)
430 50 CONTINUE
440 51 CONTINUE
450 20 CONTINUE
460 DO 60 J=1,NY
470 DO 61 I=1,NX
480 Z(I,J)=AMAX1(.9,Z(I,J))
490 Z(I,J)=AMIN1(1.1,Z(I,J))
500 61 CONTINUE
510 WRITE(13) (Z(I,J),I=1,NX)
520 60 CONTINUE

```

TABLE 1

Ellipses	Center	Major Axis	Minor Axis	Theta	Gray Level
a	(0,0)	.69	.92	0	2
b	(0,-.0184)	.6624	.874	0	-.98
c	(.22,0)	.11	.31	-18°	-.02
d	(-.22,0)	.16	.41	18°	-.02
e	(0,.35)	.21	.25	0	.01
f	(0,.1)	.046	.046	0	.01
g	(0,-.1)	.046	.046	0	.01
h	(-.08,-.605)	.046	.023	0	.01
i	(0,-.605)	.023	.023	0	.01
j	(.06,-.605)	.023	.046	0	.01

The function $f(x,y)$ as in Fig. 1 is the sum of the values of the gray levels of those ellipses a - j (with centers and axes above whose major axes makes an angle theta with the x axis measured counterclockwise) for which (x,y) is inside the ellipse.

TABLE 2

Error Distances Between Various Pairs of Reconstructions and Between Various Reconstructions and Original

In = n^{th} iteration of search; T = true or original f ;
 F = Fourier with no filtering (ϕ in (14)); \bar{F} = Fourier with
 noise filter $\phi = \bar{\phi}$ in (17).

First column are the matrices being compared, L_1 = mean
 absolute difference; L_2 = root mean square difference;
 L_3 = maximum difference; SUM = sum of the 28,800 errors
 in projection integrals of the current iteration of the
 search; MAX = maximum of the latter errors.

Matrices	L_1	L_2	L_3	SUM	MAX
I1,T	.0637	.161	.850	765	.510
I2,T	.0545	.140	.779	346	.327
I3,T	.0480	.127	.727	249	.280
I4,T	.0431	.117	.687	203	.245
I6,T	.0365	.103	.627	157	.200
I8,T	.0323	.0944	.584	136	.181
I10,T	.0296	.0883	.552	126	.169
I12,T	.0279	.0840	.526	120	.161
I14,T	.0270	.0809	.515	117	.154
I16,T	.0266	.0785	.526	116	.149
F,T	.0245	.0765	.497	-	-
\bar{F} ,T	.0352	.109	.584	-	-
I2,I1	.0165	.0309	.190	-	-
I3,I2	.0101	.0206	.125	-	-
I4,I3	.0072	.0154	.090	-	-
I8,I6	.0068	.0155	.087	-	-
I10,I8	.0050	.0116	.068	-	-
I12,I10	.0039	.0091	.054	-	-
I14,I12	.0032	.0074	.045	-	-
I16,I14	.0026	.0061	.037	-	-
I12,F	.0080	.0173	.202	-	-

TABLE 3

Reconstruction from pure noise, i.e., independent
 standard pseudo-normal projections; noise amplification
 factor A_1 is the $|\text{mean}|$, A_2 the root mean square, A_3 the
 $|\text{maximum}|$ of the 80x80 reconstructed values. F = Fourier
 method with no noise filtering, \bar{F} with noise filtering;
 In = n^{th} iteration of search. The last two rows are the
 theoretical values computed in §3 for the Fourier method.

Method	A_1	A_2	A_3
I1	.187	.282	5.039
I2	.339	.483	7.535
I3	.472	.653	9.226
I4	.591	.804	10.449
I5	.699	.940	11.352
I6	.799	1.064	12.026
I7	.891	1.178	12.532
I8	.976	1.283	12.914
I9	1.056	1.381	13.205
I10	1.130	1.473	13.426
I11	1.199	1.558	13.596
I12	1.265	1.639	13.727
F	1.672	2.099	7.8084
\bar{F}	.637	.799	3.459
F (Theory)	1.682	2.108	-
\bar{F} (Theory)	.651	.816	-

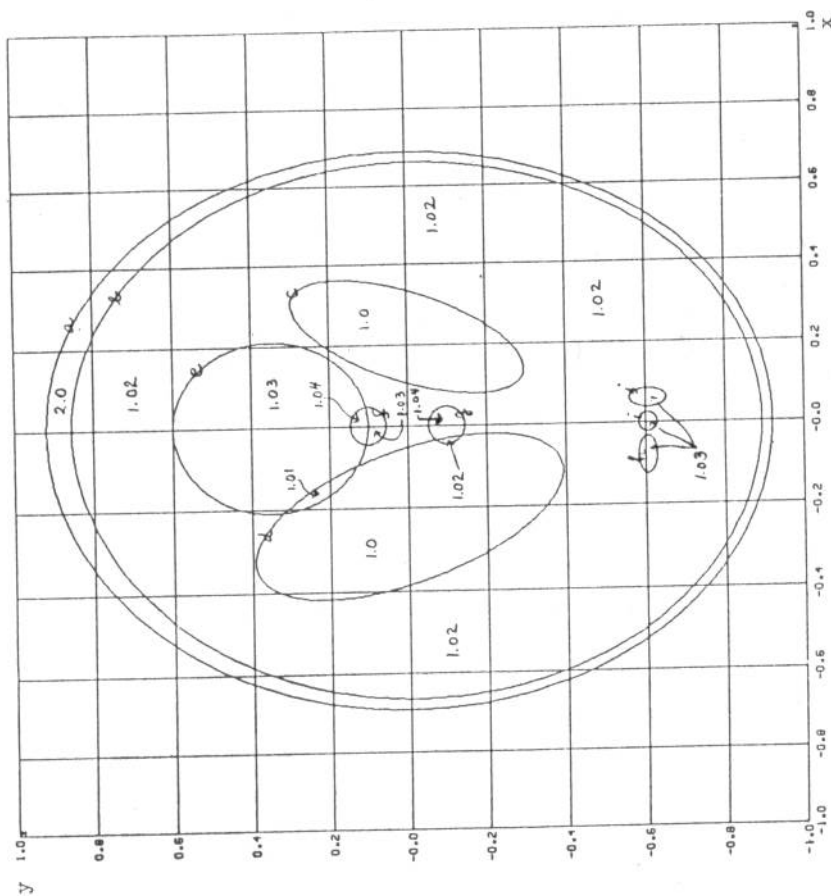


Fig. 1 The centers, axes, tilting angles, and gray levels for each ellipse are given in Table 1. In an attempt to be consistent with known facts about the human head, the skull in the figure is about twice as dense as the interior tissue and is thicker at the forehead. The ventricles filled with spinal fluid (water) are least dense (1.0, while gray matter has density 1.02 and fills the interior of the head except for tumors (1.03) at h, i, j, g , and f . Note that in the regions ($g-g'$) and e if the density is 1.04, in d (e), it is 1.01, and in d' (g) it is 1.02. In comparing dimensions with a human skull with approximate axes 10 cm. and 7.5 cm., $1 = \text{cm}$. The small circular tumor at the bottom is $\approx .5$ in diameter. Three dimensional plots of $f(x, y)$ are given in Fig. 2.

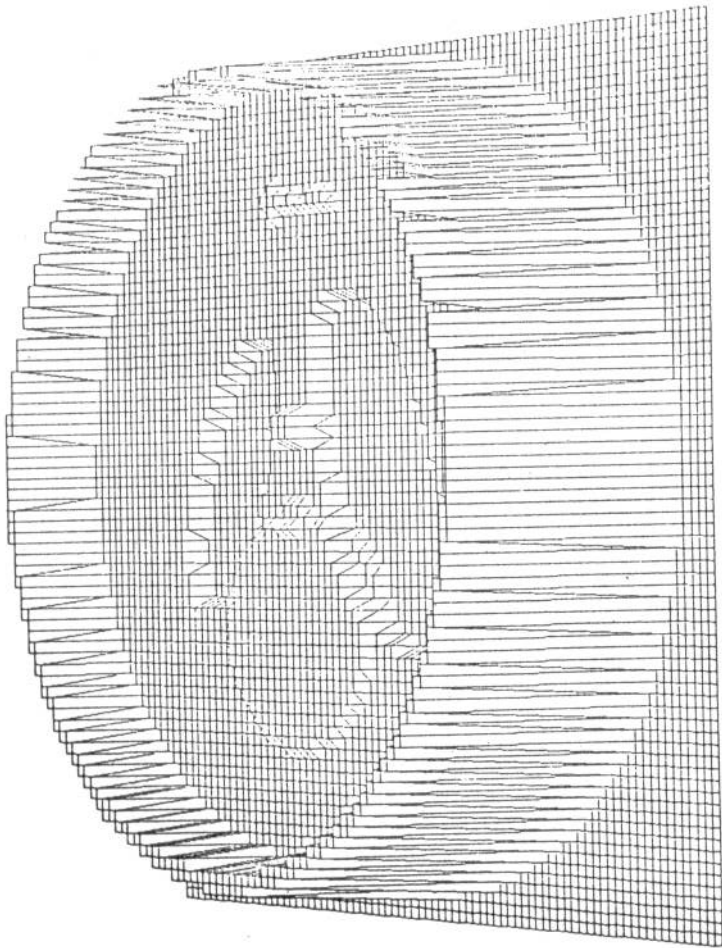


Fig. 2 The actual $f(x,y)$ in Fig. 1 80x80 perspective plot. The linear interpolation of the perspective plot intro-

$f_{\phi}(x, -.605)$

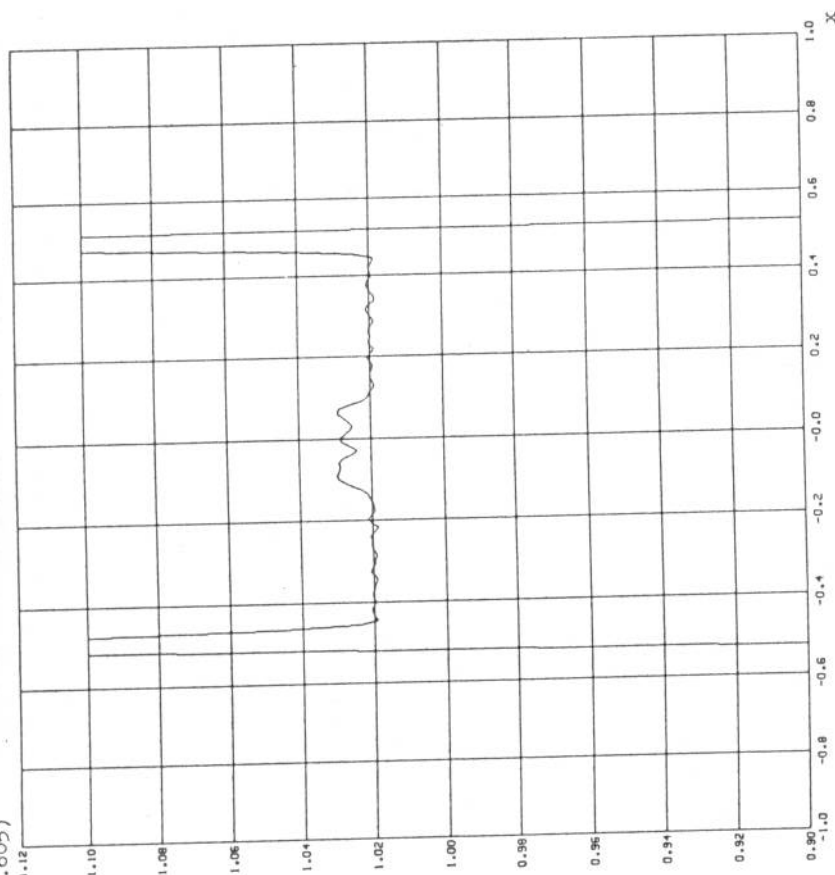


Fig. 4 Reconstruction of Fig. 3 viewed along $y = -.605$ as a function of x . This is the line through the 3 small tumors in Fig. 1. Note the gray matter etc. has been absolutely reconstructed (averaged over a small neighborhood).

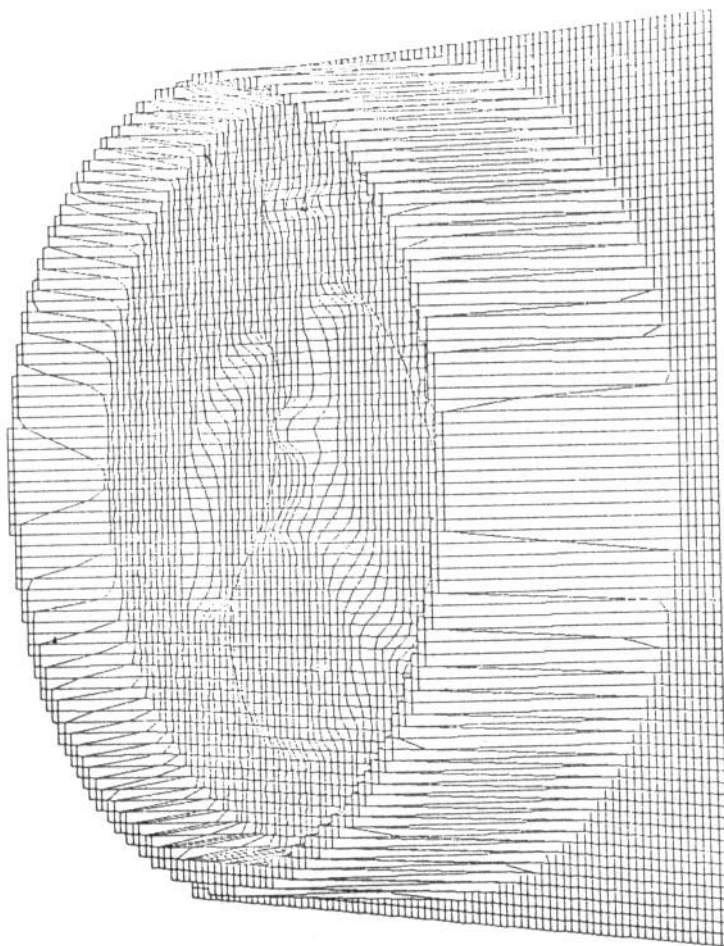


Fig. 3 Reconstruction by the Fourier algorithm with no noise from (5000) integrals over (100) abutting strips in each of 50 views. Truncated at levels .9, 1.1. Viewed from $(-10, 0, 4)$.

$f_{\phi}(x, .2)$

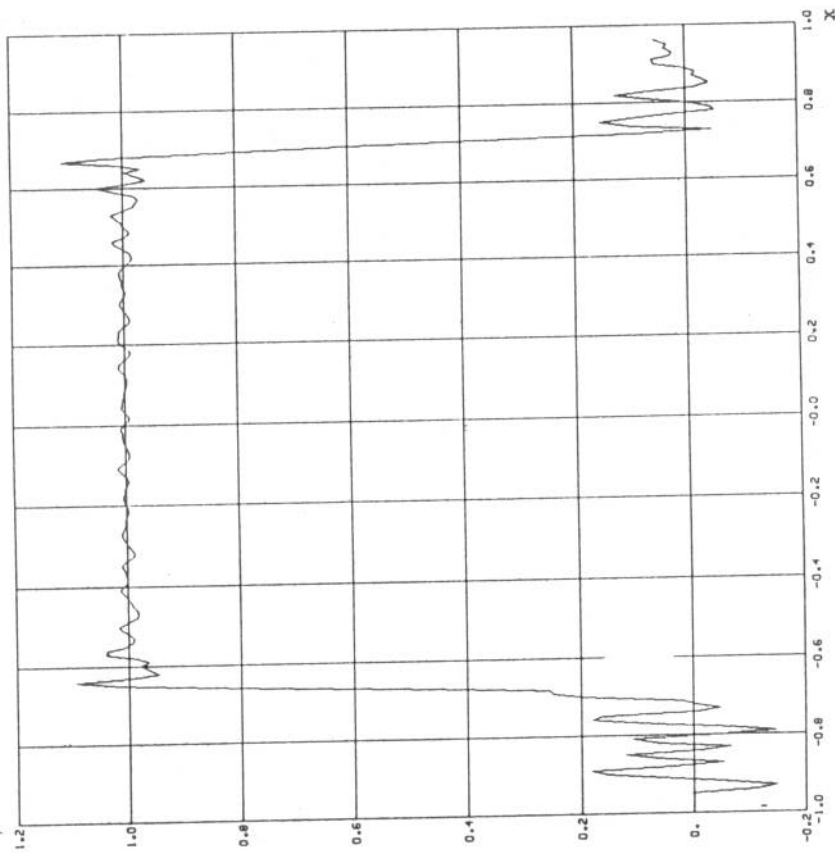


Fig. 6a Reconstruction along $y = .2$ by Fourier algorithm of a rectangle centered at origin, oriented parallel to axes, with northeast corner at $(.69, .92)$ with $n = 50$ views, $m = 100$ lines/view. The j th view is at $\theta_j = (j+.5)\pi/50$, $j = 0, 1, \dots, 49$.

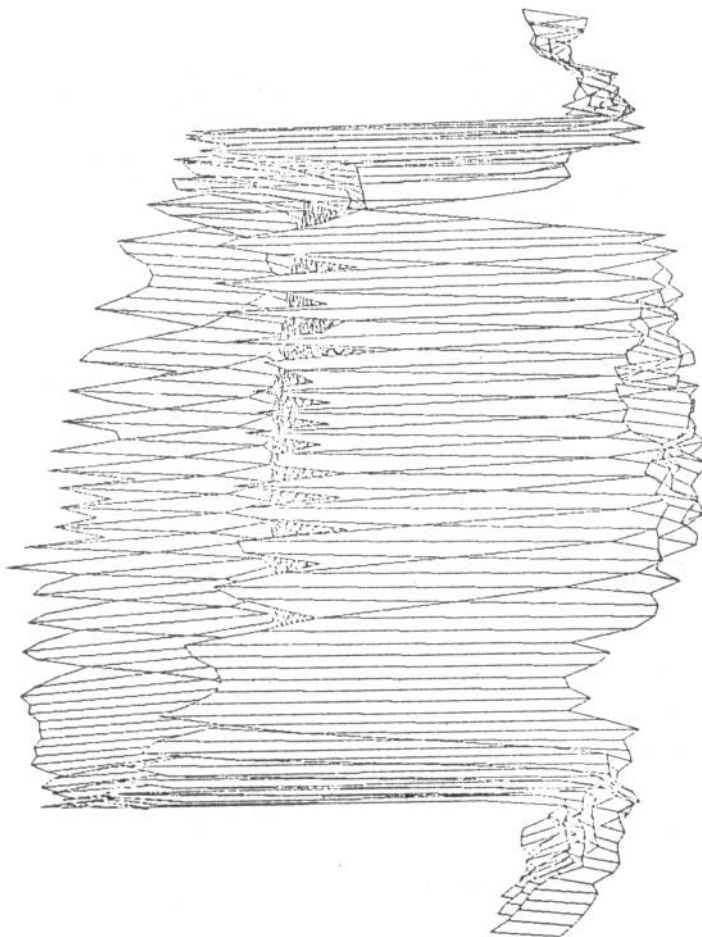


Fig. 5 Reconstruction by the Fourier algorithm of Fig. 1 without truncation at levels .9 and 1.1 as in Figs. 3-4. The variations inside the skull are hidden. The spikes are errors in the reconstruction as are the oscillations outside the skull. See discussion of figures and Appendix.

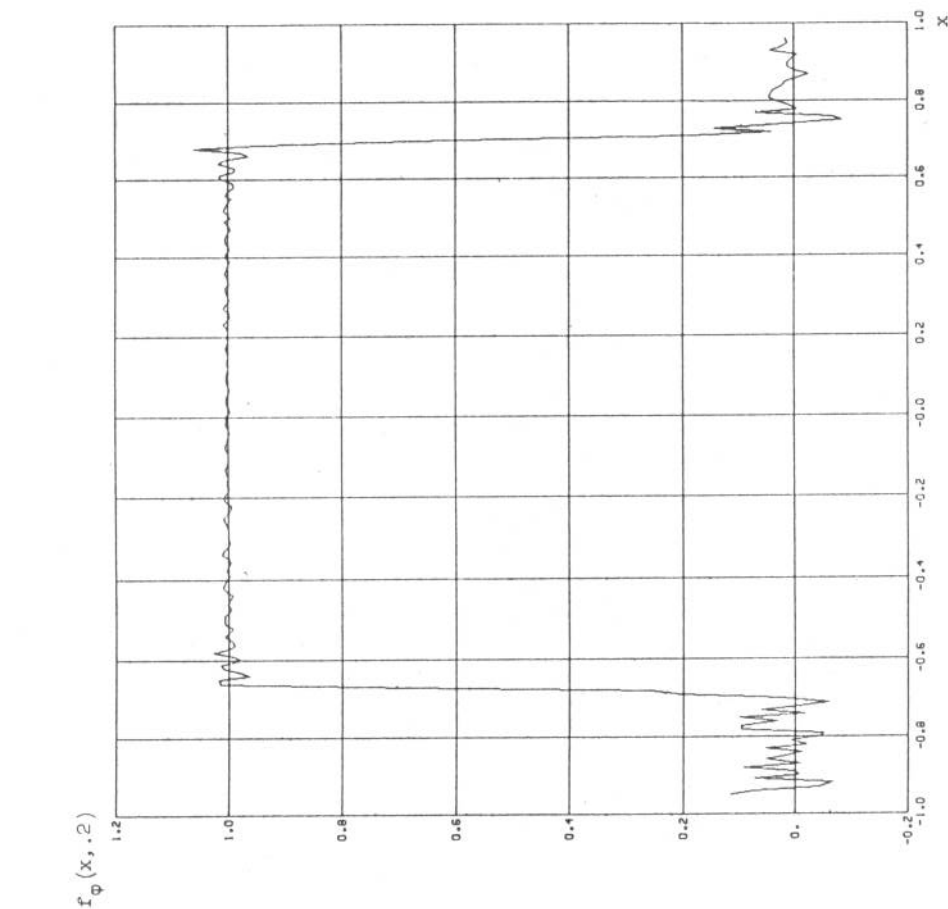


Fig. 6b Same as Fig. 6a except $n = 90$, $m = 158$.

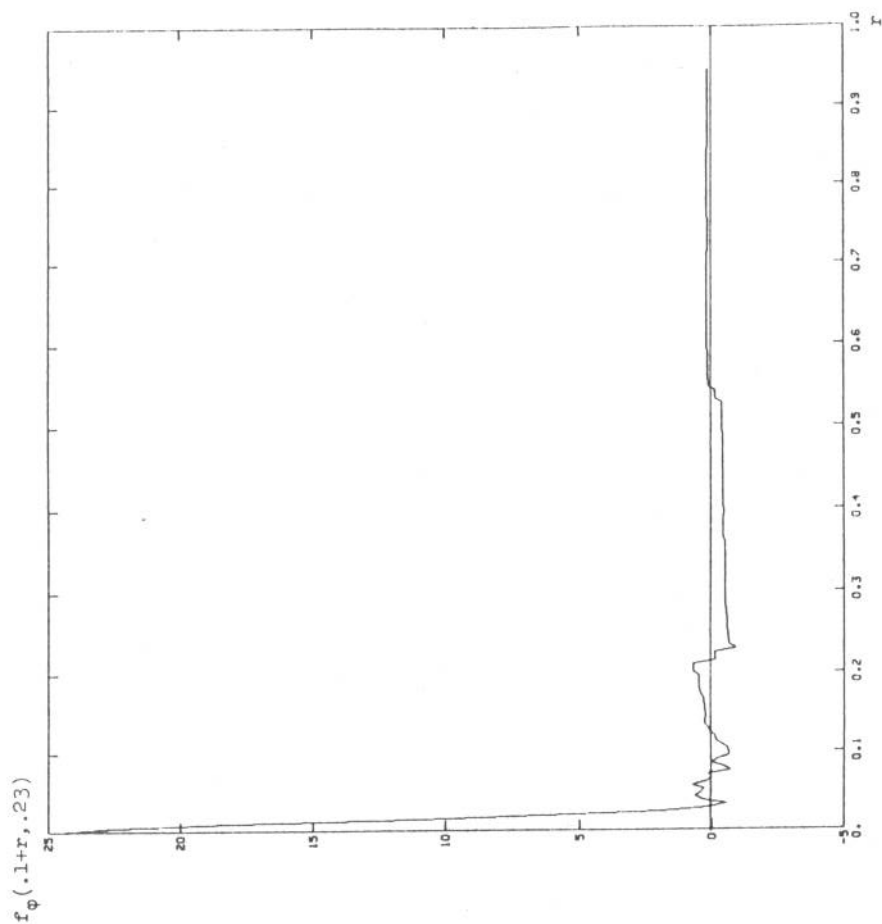


Fig. 7a The reconstruction by (12) of a δ -function f at $(.1, .23)$ from strip data along the ray $(.1+r, .23)$, $r \geq 0$. Note that the major effect is at $r = 0$ as it should be.

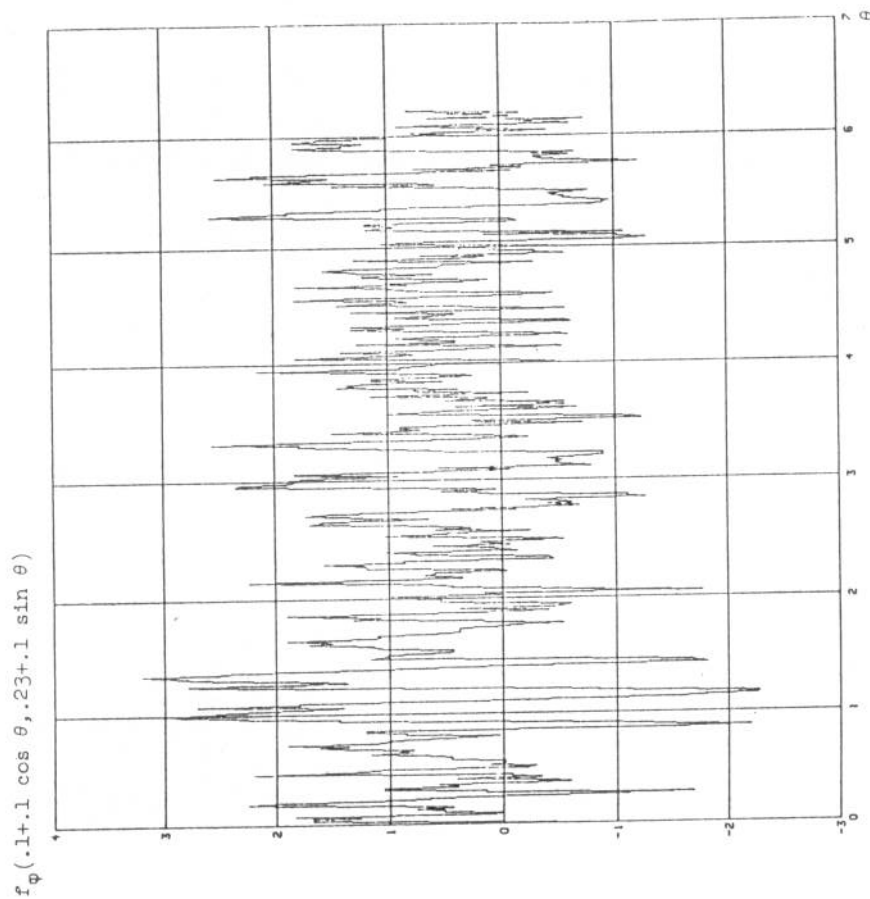


Fig. 7b Same reconstruction as in previous plot except along a circle around the point $(.1, .23)$, i.e. $f_\phi(.1+r \cos \theta, .23+r \sin \theta)$ as a function of θ , $0 \leq \theta < 2\pi = 6.28$, $r = .1$.

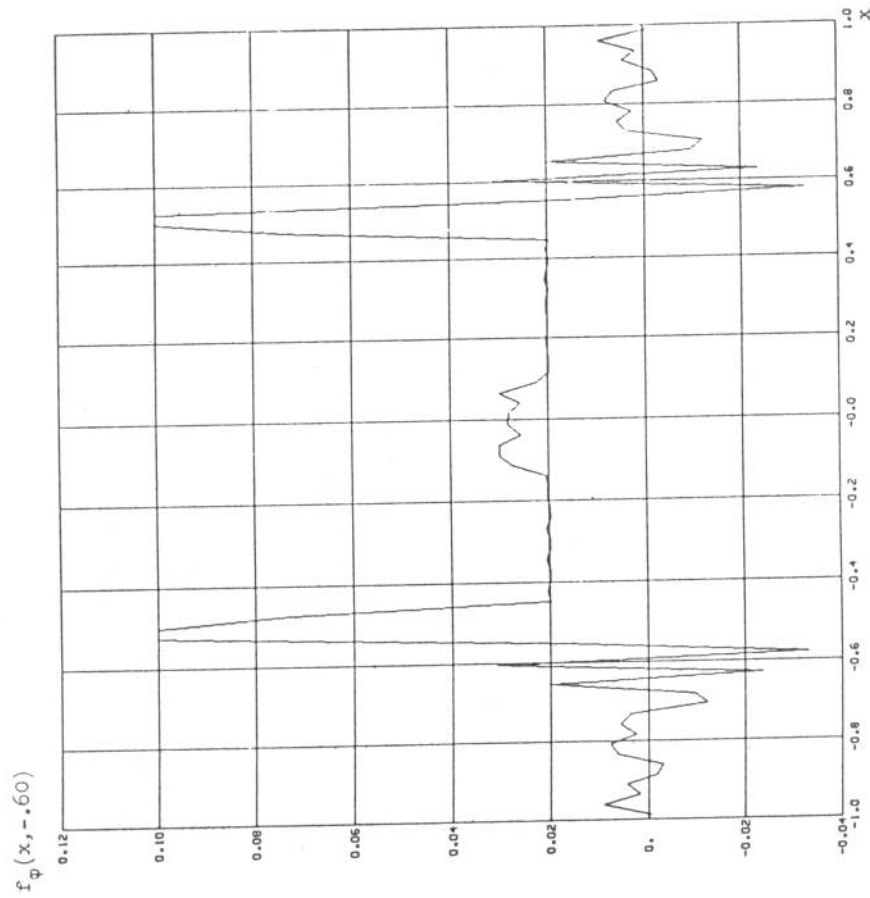


Fig. 8 Fourier reconstruction with no noise filtering of the head section of §2c with water bag and 180×160 rays as described, along $y = -.60$.

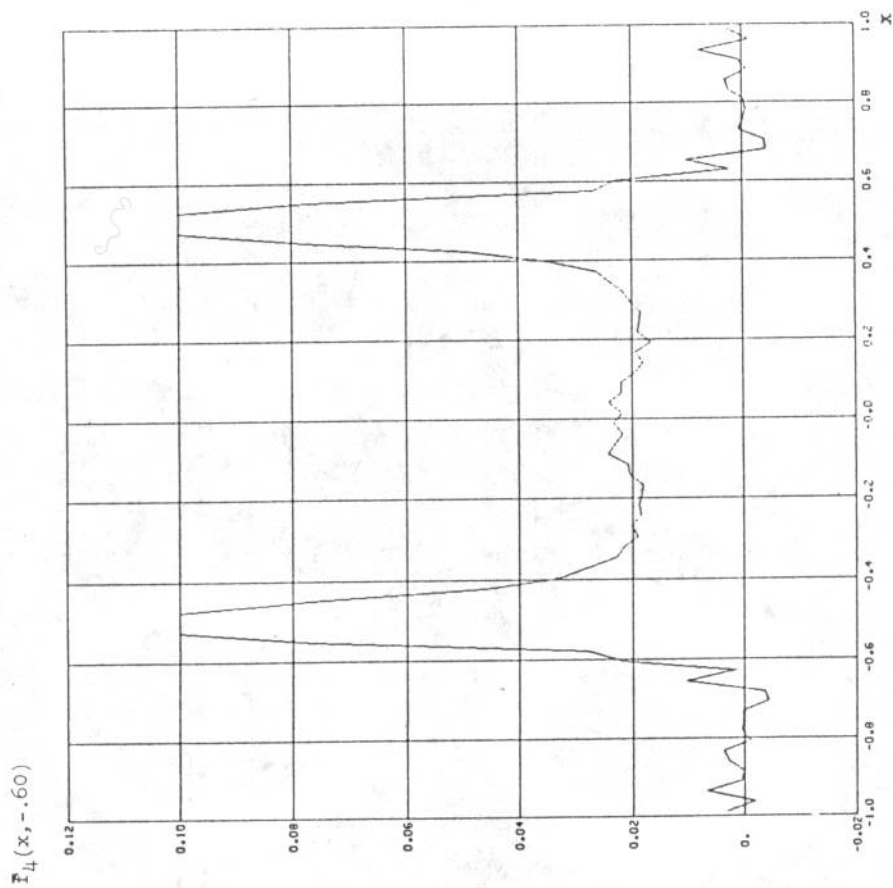


Fig. 9 4th iteration of search reconstruction from same data as in Fig. 8, along the same line, $y = -.60$, the 17th line from the bottom of the 80x80 grid.

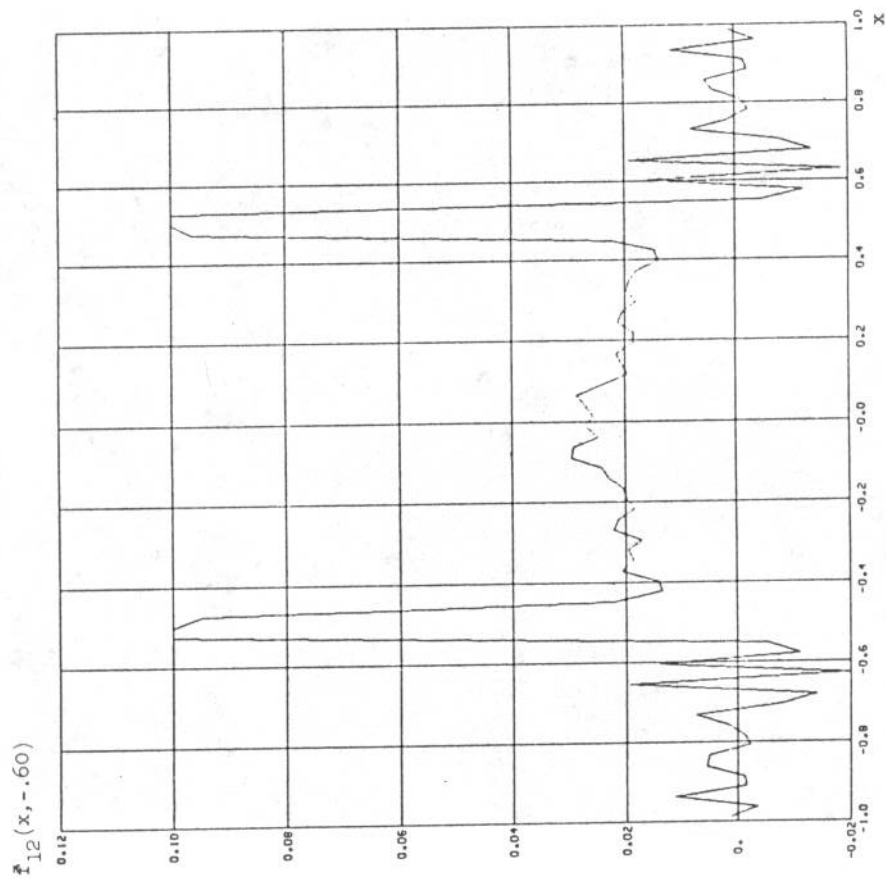


Fig. 10 12th iteration of search reconstruction from same data as in Figs. 8, 9, along the same line $y = -.60$.

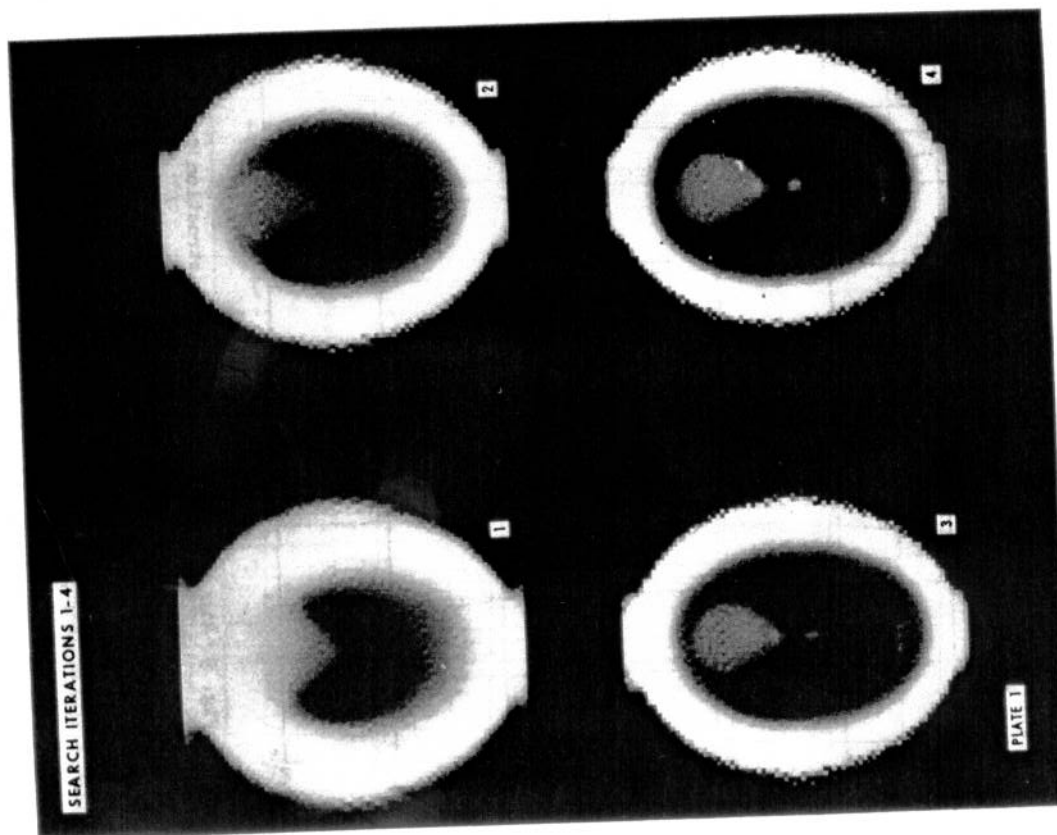


Plate 1. The first four iterations of the search algorithm under the conditions described in §2c.

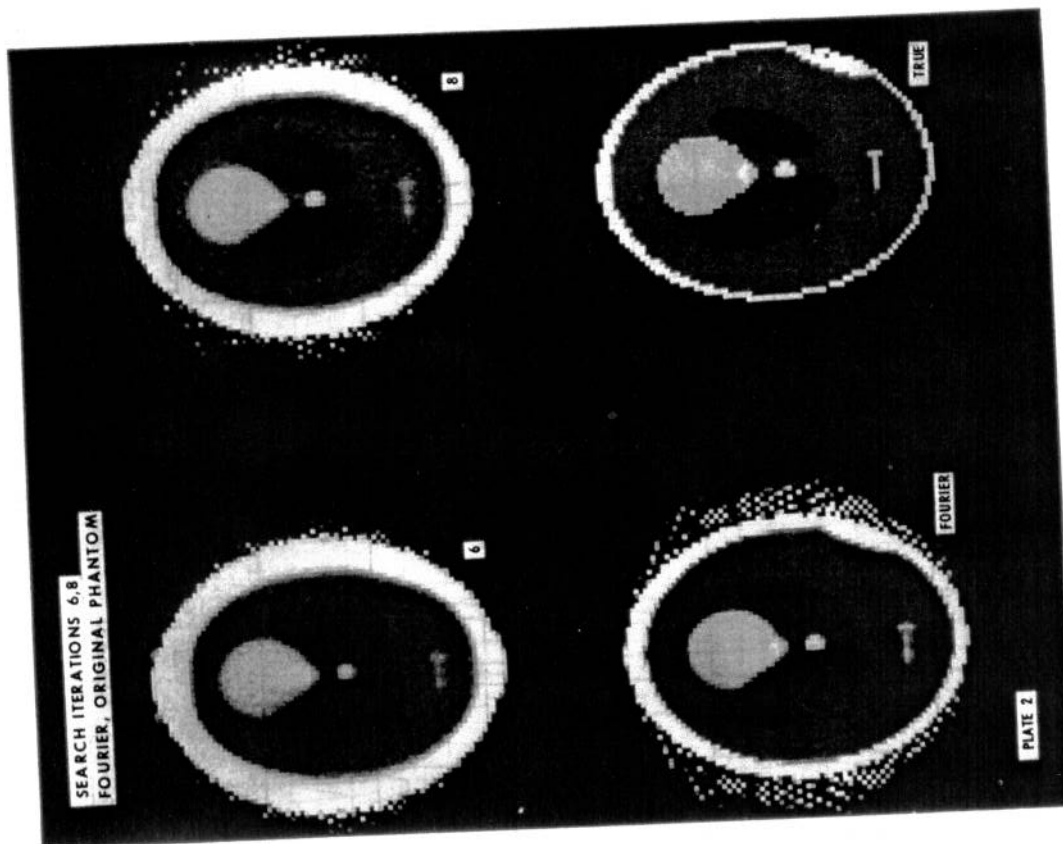


Plate 2. The 6th, 8th iterations of the search reconstruction. The Fourier reconstruction with no noise filtering. The original phantom.

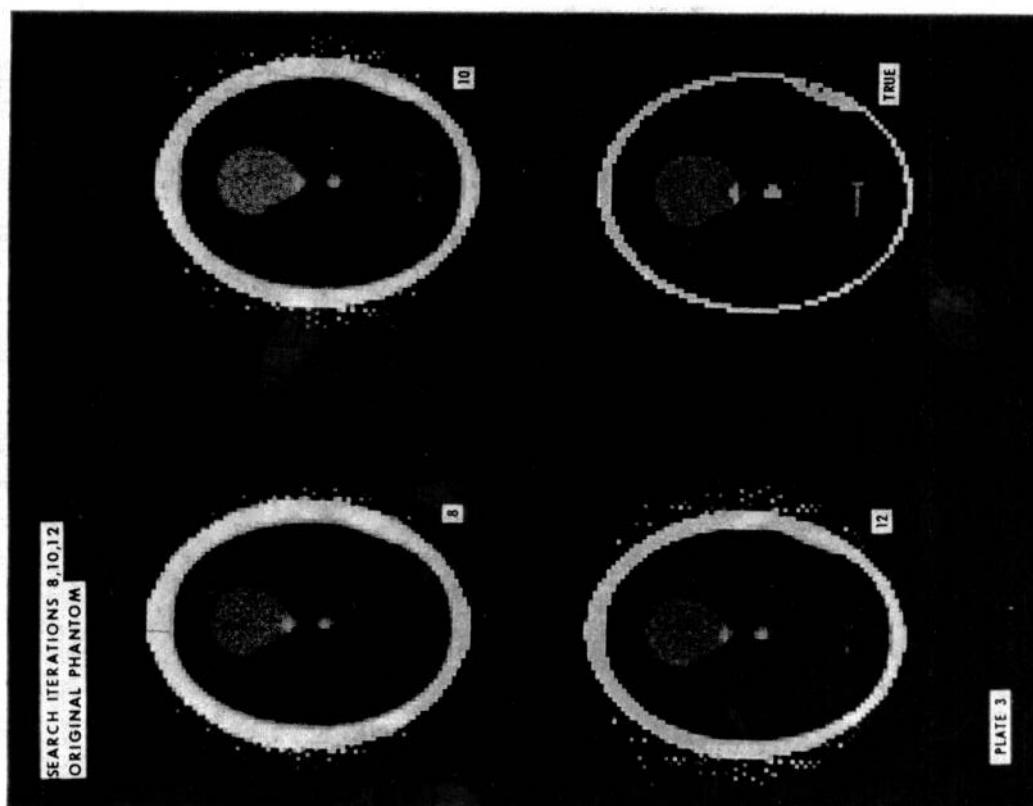


Plate 3. The 8th, 10th, 12th iterations of the search reconstruction. The original phantom. The first and last are repeats of those on Plate 2.

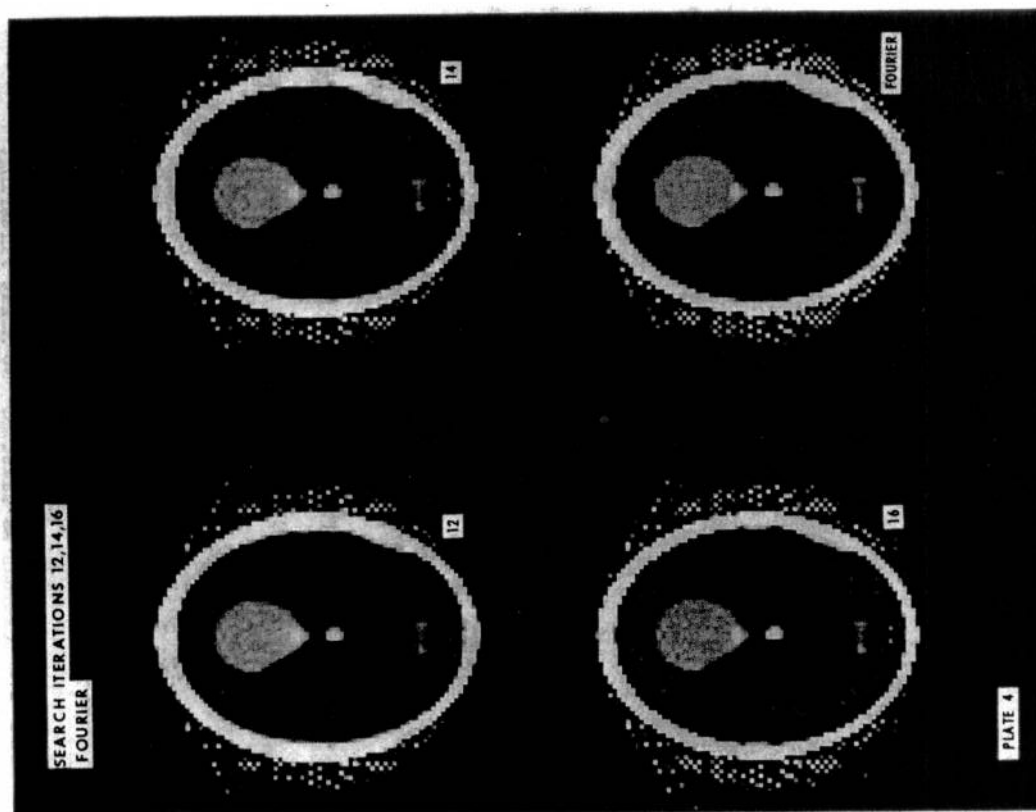


Plate 4. The 12th, 14th, 16th iterations of the search. The Fourier reconstruction with no noise filtering. The first and last are repeats of those on Plates 2, 3.

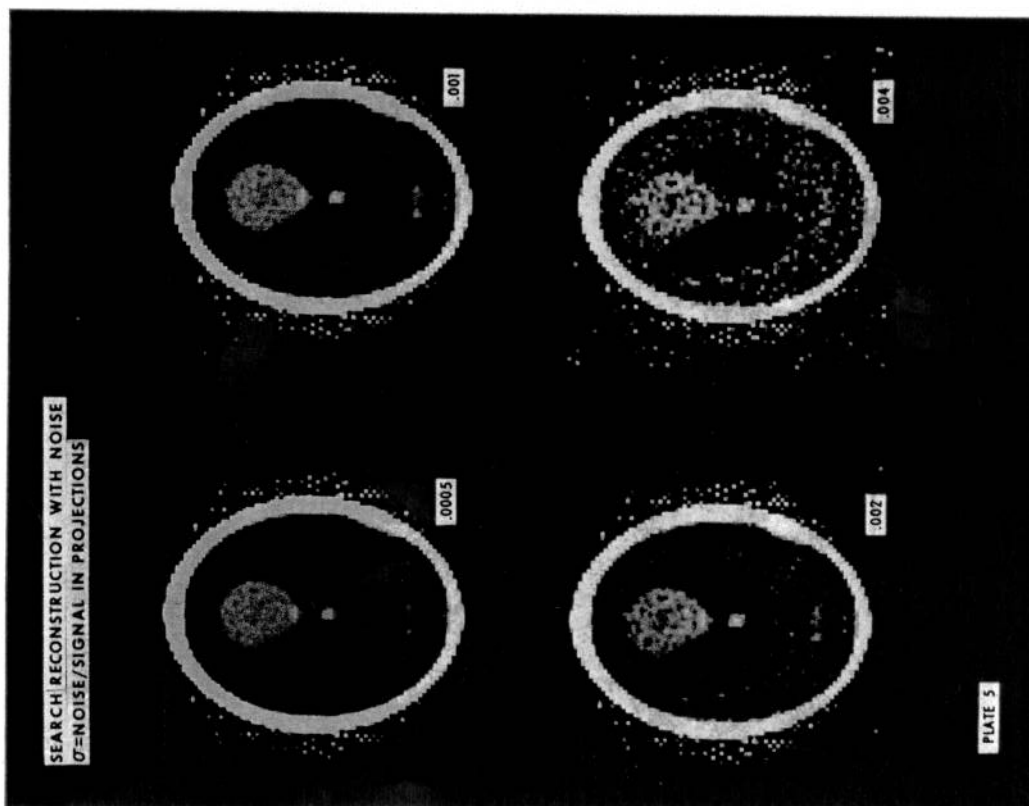


Plate 5. The search reconstruction (12 iterations) using projections with additive Gaussian noise with standard deviation $\sigma = .0005, .001, .002, .004$.

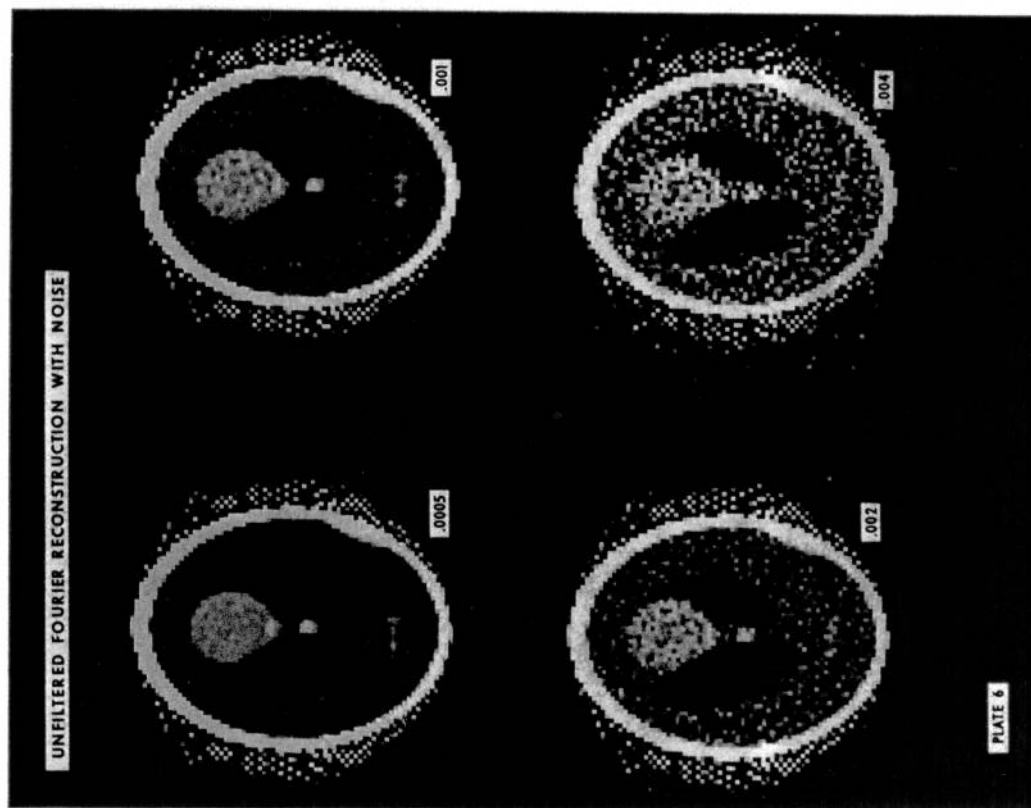


Plate 6. The Fourier reconstruction under the same conditions as Plate 5. No noise filtering.

FILTERED FOURIER RECONSTRUCTION
 σ = NOISE/SIGNAL IN PROJECTIONS



PLATE 7

Plate 7. The Fourier reconstruction under the same conditions with noise filtering. Note that the standard deviation $\sigma = .0005$ is omitted. Here $\sigma = .001, .002, .004, 0$.